Shi et al. *NPG Asia Materials* (2022) 14:87
https://doi.org/10.1038/s41427-022-00433-0

NPG Asia Materials

ARTICLE Open Access

Scalable synthesis of ultrastable lead halide perovskite-zeolite composites *via* a chemical vapor method in air

Tongyu Shi[1,2], Xi Chen[1], Yuhao Deng[1], Hao Huang[1], Jiahong Wang[1,2], Rui He[1], Yanliang Liu[1,2], Xingchen He[1], Jia Li[1], Paul K. Chu[3] and Xue-Feng Yu[1,2]

Abstract

A novel chemical vapor method is developed to synthesize ultrastable lead halide perovskite-zeolite (ZSM-5) composites, in which $CsPbX_3$ (X = Cl, Br, I) perovskite quantum dots (QDs) are grown in situ in the nanopores of the ZSM-5 substrate. The key chemical reaction between $PbBr_2$ vapor and the Si–O network in ZSM-5 leads to collapse of the initial zeolite crystal structure, realizing effective confinement and encapsulation of $CsPbBr_3$ QDs and boosting their stability under harsh conditions, including heat, water, polar solvents, and ultraviolet (UV) light. At the same time, the acquired encapsulation structure possesses the channels needed for halogen exchange to regulate the halide ratios of the $CsPbX_3$-ZSM-5 composites. The synthesized $CsPbX_3$-ZSM-5 composites exhibit tunable emission from 400 to 700 nm and narrow full-widths at half-maximum (FWHM). To demonstrate the commercial potential, $CsPbX_3$-ZSM-5 composites synthesized on a large scale are applied in white light-emitting diodes (WLEDs) and multicolor-coded anti-counterfeiting inks.

Introduction

$CsPbX_3$ (X = Cl, Br, I) QDs are emerging semiconductor materials and have attracted increasing attention due to their high defect tolerances, charge carrier mobilities, tunable bandgaps, and long carrier diffusion lengths[1,2]. Numerous recent reports have demonstrated the advantages of $CsPbX_3$ QDs over conventional semiconducting materials[3]. In particular, their high photoluminescence quantum yields (PLQYs), narrow emission widths, and wide color range make them competitive candidates for lighting, backlight display, and anti-counterfeiting applications[3]. As photoluminescent layers, $CsPbX_3$ QDs have been used in WLEDs and anti-counterfeiting coatings exhibiting high performance[4]. To accelerate practical use of $CsPbX_3$ QDs, a great deal of research on crystal structures and fabrication strategies has been carried out, and remarkable progress has been achieved[5]. However, it is still challenging to use $CsPbX_3$ QDs as commercial materials because of the drawbacks of prevalent synthetic methods, which usually involve large amounts of organic solvents, ligands, inert gas protection, and tedious cleaning and purification processes, thereby rendering them unsuitable for environmentally friendly and scalable production[6,7]. In addition, the stabilities of colloid QDs prepared by using solvents are generally mediated by large organic ligands, but unfortunately, the highly dynamic surfaces of QDs might cause desorption of ligands, resulting in structural damage and performance degradation of the ionic $CsPbX_3$ QDs due to moisture or thermal attack[8,9].

Great effort has been expended to overcome the instability issues, and various passivation strategies have

Correspondence: Hao Huang (hao.huang@siat.ac.cn) or Xue-Feng Yu (xf.yu@siat.ac.cn)
[1]Shenzhen Engineering Centre for the Fabrication of Two-Dimensional Atomic Crystals, Shenzhen Institute of Advanced Technology, Chinese Academy of Sciences, Shenzhen 518055, People's Republic of China
[2]University of Chinese Academy of Sciences, Beijing 100049, People's Republic of China
Full list of author information is available at the end of the article
These authors contributed equally: TongYu Shi, Xi Chen

been proposed, such as surface engineering and matrix encapsulation[10]. Mohammed et al. found that ligands with $-NH_3^+$ groups strongly bound to Br^- ions on specific surfaces of $CsPbBr_3$ (110) and enhanced the PL intensity and stability[11]. Compared with ligand modification methods, the inert encapsulation technique showed greater potential for preparing ultrastable perovskite composites. Oxides (SiO_2[12], SiO_2/AlO_x[13], molecular sieves[14–16]), semiconductors (ZnS[17] and $Pb_4S_3Br_2$[18]), polymers (polydimethylsiloxane[19] and polystyrene[20]), and metal-organic frameworks (PCN-333(Fe)[21] and UiO-66(NH_2)[22]) have served as effective matrix materials. Y Lin et al. reported the preparation of $CsPbX_3/SiO_x$ by high-temperature sintering synthesis, and the humidity and heat resistance were significantly improved[12]. Wang et al. successfully synthesized an ultrastable perovskite composite based on the aluminophosphate AIPO-5, which provided confinement for growth of the nanocrystals, defect passivation, and robust barrier surroundings[15]. In addition to the enhanced stability, the absolute PL intensities of $CsPbX_3$-a_gZIF-62 composites are often at least two orders of magnitude higher than those of the corresponding pure $CsPbX_3$[23]. In view of the significant breakthroughs in the stabilities of $CsPbX_3$ QDs, the problems with scalable preparation should be considered because complicated postprocessing steps are inevitable in the strategies mentioned above[24].

The solvent-free chemical vapor method is commonly applied in scalable syntheses of functional films, nanotubes, and catalysts due to its relatively low reaction temperatures, flexible product compositions, broad application range, and extraordinary diffusion ability[25,26]. Molecular sieves are typical active porous materials, and they allow gases and small molecules to pass through their unique channel structures; these are ideal accessory ingredients and support materials in various synthetic reactions[27,28]. Herein, a novel chemical vapor method is designed and demonstrated for scalable production of $CsPbX_3$ composites with superior optical properties and ultrahigh stabilities. By employing ZSM-5 as the porous template and taking advantage of special reactions between $PbBr_2$ vapor and the Si–O network of ZSM-5, in situ growth of $CsPbX_3$ QDs confined in the nanometer-scale space is achieved without organic solvents and ligands. Additionally, the acquired encapsulation structure has the channels needed for halogen exchange to regulate the halide ratios of the $CsPbX_3$-ZSM-5 composites. Consequently, the $CsPbX_3$-ZSM-5 composites can be mass-produced with high PLQYs and narrow emission FWHM. In addition, owing to the protection and isolation provided by inert ZSM-5, the $CsPbX_3$ QDs are prevented from agglomerating and regrowing, and the composites exhibit exceptional stability under harsh conditions, including heat, water, polar solvents, and UV light. To demonstrate practical viability, the composites are applied in WLEDs with a large color range and multicolor-coded anti-counterfeiting inks.

Materials and methods

Materials and chemicals

$PbBr_2$ (lead bromide, 99%, Shanghai Aladdin Biochemical Technology Co., Ltd., China), CsBr (cesium bromide, 99.5%, Aladdin), ZSM-5 molecular sieves (SiO_2/Al_2O_3, molar ratio ~ 40–50, Aladdin), tetrabutylammonium chloride (TBAC, 97%, Aladdin), and tetrabutylammonium iodide (TBAI, 99%, Aladdin) were used as received without further purification.

Synthesis of $CsPbX_3$-ZSM-5 composites

The green-emission composite was synthesized via a facile one-step vapor diffusion method. CsBr and $PbBr_2$ were weighed to give a 1:1 stoichiometric ratio, and an appropriate amount of ZSM-5 was added (designed mass ratio of (CsBr+$PbBr_2$): ZSM-5 = 1:2). The mixture was calcined at 650 °C for 300 min with a heating rate of 10 °C min^{-1} and then cooled to 30 °C in a muffle furnace in air. The processes used to prepare materials with different proportions were similar. $CsPbBr_xCl_{3-x}$-ZSM-5 and $CsPbBr_xI_{3-x}$-ZSM-5 with different halogen compositions were synthesized via ion exchange by mixing and grinding the $CsPbBr_3$-ZSM-5 powder with a certain amount of tetrabutylammonium iodide or tetrabutylammonium chloride and then calcining at 250 °C for 300 min to obtain $CsPbBr_xCl_{3-x}$-ZSM-5 and $CsPbBr_xI_{3-x}$-ZSM-5.

Syntheses of ZSM-650, CsBr-ZSM, $PbBr_2$-ZSM

ZSM-650 was prepared by annealing ZSM-5 at 650 °C. CsBr-ZSM was prepared by mixing CsBr with ZSM-5 (mass ratios from 1:2 to 2:1) and then annealing at 650 °C. Similarly, $PbBr_2$-ZSM was prepared by mixing $PbBr_2$ with ZSM-5 (mass ratios from 1:4 to 1:1) and then annealing at 650 °C.

Characterization

The morphologies and microstructures of the $CsPbX_3$-ZSM-5 composites were examined by scanning electron microscopy (SEM, Zeiss GeminiSEM 300) and transmission electron microscopy (TEM, FEI Talos F200X) at 200 kV. The compositions of the composites were determined by energy-dispersive X-ray spectroscopy (EDS) using an accessory manufactured by Oxford Instruments. To characterize structures, powder X-ray diffraction (XRD) studies were performed with a Rigaku Smartlab 3 kW X-ray diffractometer with Cu K_α radiation ($\lambda = 1.54056$ Å, 40 kV, 30 mA, 10° min^{-1} from 5 to 80°). X-ray photoelectron spectroscopy (XPS) was carried out on a Thermo ESCALAB 250Xi system. The structures of the composites were analyzed by Fourier transform

infrared spectroscopy (FTIR, Thermo Scientific, Nicolet iS60) with the KBr pellet method. PL properties were investigated on a fluorescence spectrophotometer (Hitachi F-4600) with an excitation wavelength of 365 nm, and UV−Vis spectra were recorded on an ultraviolet spectrometer (AOE Instruments, UV-A390). Thermal properties were determined by simultaneous thermal analyses (ZCT-B TG/DTA) run at a heating rate of 10 °C min^{-1} in air, and micropore analyses, including surface areas and pore volumes, were conducted with a Micro Active ASAP 2460 system.

PLQY measurements

The composite powders were dispersed in glycol to prepare samples. Samples were photoexcited at an excitation wavelength of 365 nm, and a spectrophotometer (FLS 1000, Edinburgh, UK) was used for PLQY analysis.

Fabrication of WLEDs

WLEDs were fabricated by combining synthesized green-emission and red-emission perovskite composites with blue LED chips. The composites were mixed with epoxy resin by vigorous stirring, dropped onto the chip and cured at 80 °C. The devices were characterized using a Keithley 2450 system as a current source, and the output spectra were recorded with an HP-8000 LED fast-scan micro-spectrophotocolorimeter.

Stability evaluation

Water and polar solvent stability tests were performed by dispersing the powders directly in the solvents. The samples for stability tests involving heating, aging, and continuous radiation were prepared by putting solutions of $CsPbX_3$-ZSM-5 composites onto quartz plates to form films. The films were exposed to a heating plate under aging conditions of 80 °C and 80% relative humidity in a constant temperature and humidity incubator as well as continuous UV light illumination (365 nm) separately. Photoluminescence spectra were acquired after different testing conditions using a fluorescence spectrometer.

Results and discussion

Chemical vapor syntheses of $CsPbX_3$-ZSM-5 composites

A novel chemical vapor technique with advantages such as stability in an air atmosphere, operation without organic solvents, and scalability was developed to produce commercially available $CsPbX_3$ composites. As illustrated in Fig. 1a, CsBr and $PbBr_2$ were placed separately at the bottom of a ceramic crucible and covered by a layer of ZSM-5 particles and then annealed in an air atmosphere with a programmed temperature. After cooling the furnace to room temperature, a $CsPbBr_3$-ZSM-5 composite exhibiting bright green emission was obtained and named Green-Z, The SEM image and elemental maps in Fig. 1b and Fig. S1 in the Supplementary Information suggest the formation of $CsPbBr_3$. The detailed SEM images of pristine ZSM-5 (Fig. 1c) and Green-Z (Fig. 1d) clearly showed the great morphological changes of ZSM-5 particles from a regular square shapes to a smooth and round surfaces. According to the transmission electron microscopy (TEM) image (Fig. 1e), the isolated $CsPbBr_3$ QDs were distributed uniformly in the matrix. A high-angle annular dark-field (HAADF) image and elemental maps are presented in Fig. 1f. It is known that TEM contrast is commonly limited by the thicknesses of samples or matrices with high density, and incomplete information is sometimes provided by TEM images. Unlike TEM, HAADF image intensities are approximately proportional to the square of the atomic number of the substance, so HAADF images are less affected by the surrounding medium[29]. The HAADF image contrast was consistent for the different atoms in ZSM-5 and $CsPbBr_3$ QDs, and the average size of the $CsPbBr_3$ QDs was 6.40 nm. It should be noted that when the ($CsBr+PbBr_2$) proportion increased, the signal from $CsPbBr_3$ increased, and the color of the composite became deeper (Fig. S2, Supplementary Information); however, when the $CsPbBr_3$ was overloaded, it grew on the surfaces of ZSM, which was investigated by immersing the composites in water. Samples 6# and 7# showed deeper colors and certain amounts of perovskite on their surfaces before immersion in water and became whiter powders with porous structures after immersion in water, while the other samples showed little change (Fig. S3, Supplementary Information).

$CsPbX_3$-ZSM-5 samples with different halide ratios and emission colors were prepared by vapor halogen exchange, as Fig. 2a illustrates. The synthesized Green-Z composite acted as a raw material and was heated to 250 °C together with tetrabutylammonium halide. The PL emission of $CsPbX_3$-ZSM-5 was tunable with the halide ratio, and three typical samples exhibiting bright green, blue and red emission under UV light are shown in Fig. 2a. The elemental maps in Fig. 2b and Figs. S4 and S5 in the Supplementary Information also indicated successful halogen exchange. Despite the different emission colors, different $CsPbX_3$-ZSM-5 samples, designated Red-Z, Orange-Z, Yellow-Z, Turquoise-Z, Blue-Z, and Purple-Z, had similar morphologies (Fig. 2c), demonstrating that halogen exchange did not change the morphology of Green-Z. Moreover, the structures of the composites were characterized by XRD (Fig. 2d). The peaks from the Green-Z composite were indexed to $CsPbBr_3$ (PDF#18-0364) and ZSM-5 (PDF#44-0003). Slight shifts in the perovskite diffraction peaks from the other six samples were also observed, which showed that halogen exchange in the vapor phase was effective. For example, the shifts of peaks from Red-Z to the left reflected an increase in interplanar spacing caused by the larger radii of I^- ions,

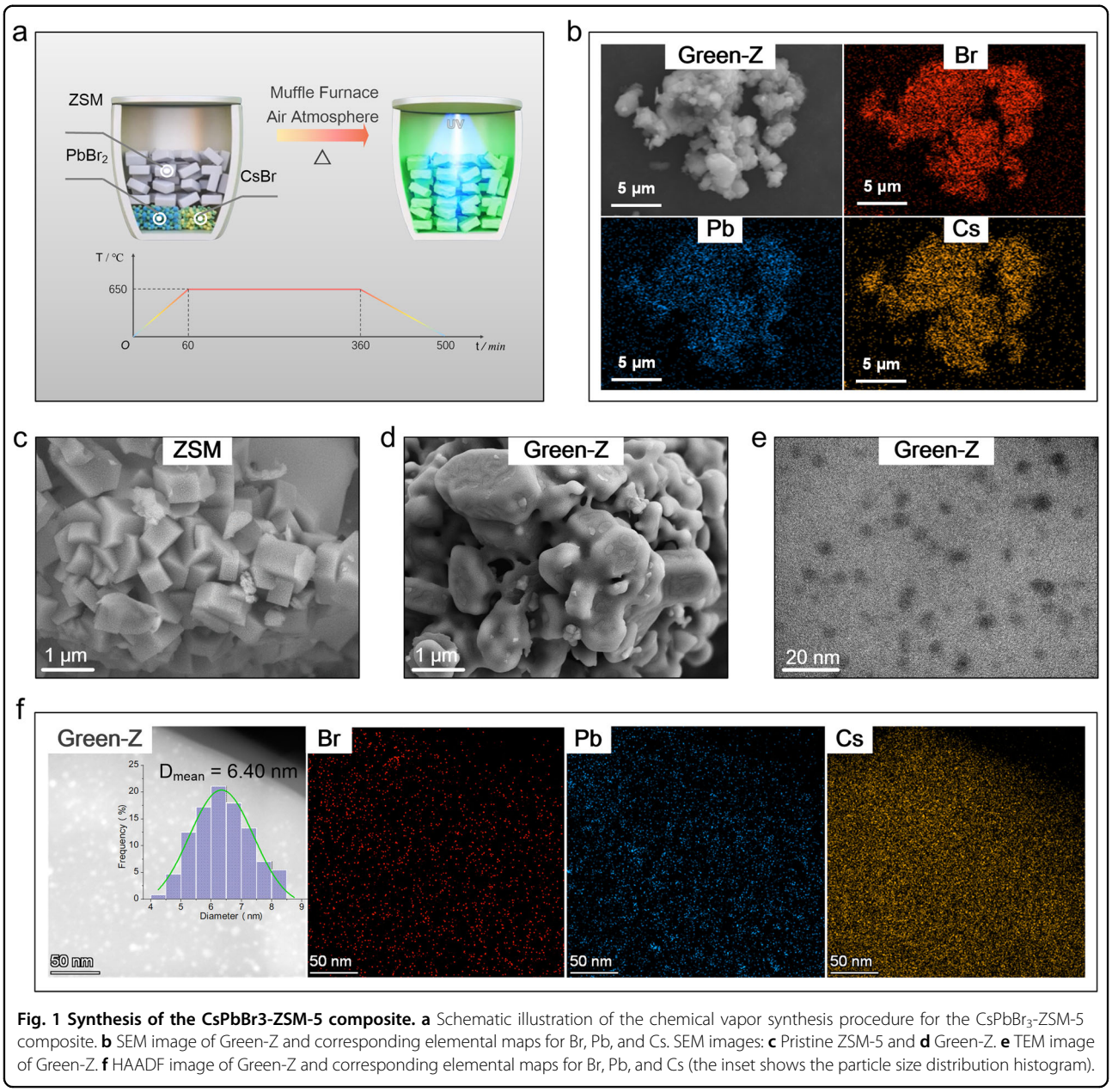

Fig. 1 Synthesis of the CsPbBr3-ZSM-5 composite. a Schematic illustration of the chemical vapor synthesis procedure for the $CsPbBr_3$-ZSM-5 composite. **b** SEM image of Green-Z and corresponding elemental maps for Br, Pb, and Cs. SEM images: **c** Pristine ZSM-5 and **d** Green-Z. **e** TEM image of Green-Z. **f** HAADF image of Green-Z and corresponding elemental maps for Br, Pb, and Cs (the inset shows the particle size distribution histogram).

while Purple-Z showed the opposite effect. The diffraction signals from $CsPbX_3$ were weaker than those from ZSM-5 due to the large size differences between the nanoscale $CsPbX_3$ dispersed in the pore channels and the micron-scale ZSM-5 matrix.

Mechanism of chemical vapor synthesis

Experiments were designed to elucidate the mechanism for the formation of the $CsPbX_3$-ZSM-5 composites. First, pristine ZSM-5, a mixture of CsBr and ZSM-5 and a mixture of $PbBr_2$ and ZSM-5 were annealed at 650 °C and named ZSM-650, CsBr-ZSM (1:2), and $PbBr_2$-ZSM (1:2), respectively. SEM images of the three samples are shown in Fig. 3a. ZSM-650 and CsBr-ZSM showed no significant difference compared with pristine ZSM-5 (Fig. 1c); however, $PbBr_2$-ZSM was similar to Green-Z (Fig. 1d) with obvious etching tracks. Then, other lead compounds, such as PbO, $Pb(CH_3COO)_2$, and $Pb(NO_3)_2$, were also annealed at 650 °C together with ZSM-5, but a similar etching phenomenon was not observed (Fig. 3a and Fig. S6 in the Supplementary Information), indicating the indispensable synergistic role of Pb^{2+} and Br^- in the structural evolution. In addition to the morphological evidence, XRD patterns (Fig. 3b, Figs. S7 and S8 in the Supplementary

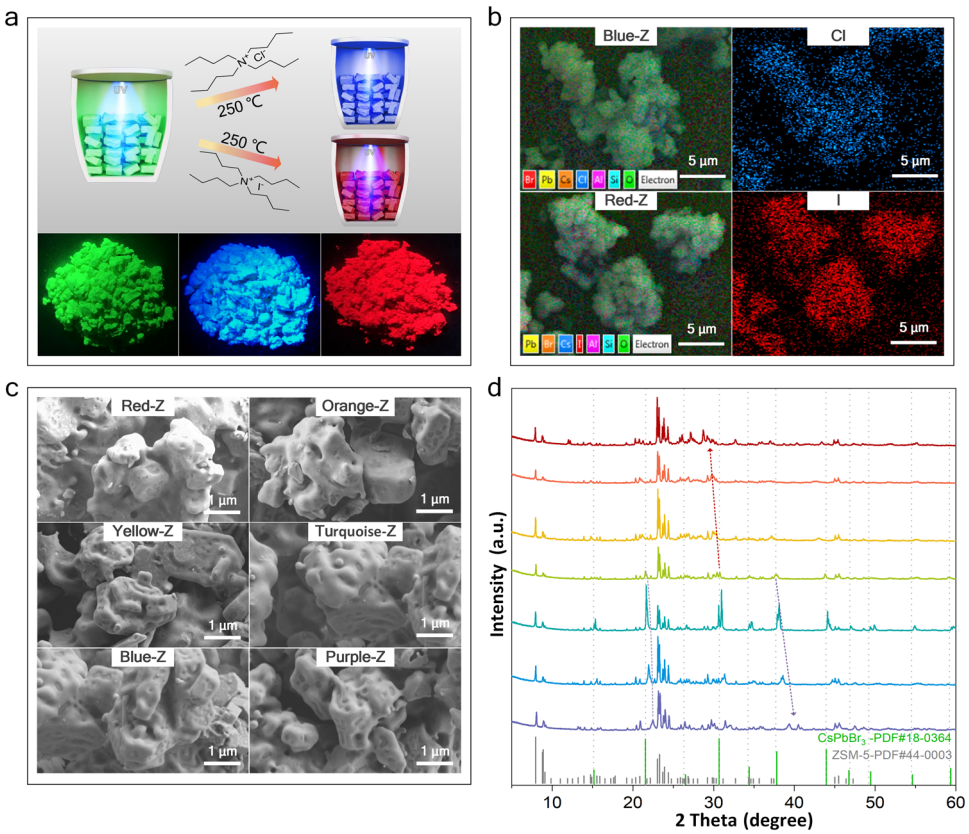

Fig. 2 Syntheses of CsPbX3-ZSM-5 composites. a Schematic illustration of the vapor halogen exchange and photographs of Green-Z, Blue-Z, and Red-Z under UV excitation at 365 nm. **b** Elemental maps for typical Blue-Z and Red-Z samples. **c** SEM images and **d** XRD patterns for multicolor $CsPbX_3$-ZSM-5 composites.

Information) further confirmed the unique effect of $PbBr_2$ that prompts the crystal structure of ZSM-5 to collapse and become amorphous, and the more $PbBr_2$ there was, the more obvious the collapse. It should be noted that with further increases in the mass ratio of CsBr to ZSM (from 1:2 to 2:1), the morphology and crystallinity of ZSM were still maintained (Figs. S9 and S10 in the Supplementary Information).

To study the reaction process, Fourier transform infrared (FTIR) spectroscopy (Fig. 3c and Fig. S11 in the Supplementary Information) was carried out. The vibrational peaks for Si–O–Si systems appeared at 543 cm^{-1} (double five-ring vibrations in the ZSM-5 framework) and 795 cm^{-1} (internal symmetric stretching vibrations, which are also observed for silica)[30,31], and the peak at 620 cm^{-1} (double tetrahedral rings in the ZSM-5 framework)[30] for ZSM-5 as well as the weak broad band from 3648 to 3655 cm^{-1} for –OH of Si–OH moieties were also observed. The pristine ZSM-5 and CsBr-ZSM samples exhibited similar spectra. However, the spectrum for $PbBr_2$-ZSM differed in that the peak at 620 cm^{-1} and the bands for Si–OH were extremely weak. In particular, the peak at 543 cm^{-1} for vibrations of double five-rings in the ZSM-5 framework disappeared, indicating that the structure of ZSM-5 had changed. Small changes in the peak at 795 cm^{-1} were ascribed to the internal symmetric stretching vibrations of silica, which resisted structural modification[31]. Based on these results, it is proposed that $PbBr_2$ might react with the Si–OH species in ZSM-5 and contribute to breakage of the matrix structure.

To verify this hypothesis, differential thermal analyses (DTA) were performed, and the curves are shown in Fig. 3d. No peak was observed for ZSM-5 because of its high thermal stability, and the one endothermic peak at 628 °C from CsBr-ZSM corresponded to the melting point of CsBr. For $PbBr_2$-ZSM, the endothermic peak at 370 °C was due to melting of the $PbBr_2$, and the peak at ~525 °C suggested an endothermic process that might be a reaction between $PbBr_2$ and ZSM-5. To simulate the main synthetic processes, the DTA curve for a mixture of CsBr, $PbBr_2$, and ZSM-5 (Fig. S12a in the Supplementary Information) was measured and compared with that for pure $CsPbBr_3$ (Fig. S12b in the Supplementary Information). In Fig. S12a in the Supplementary Information,

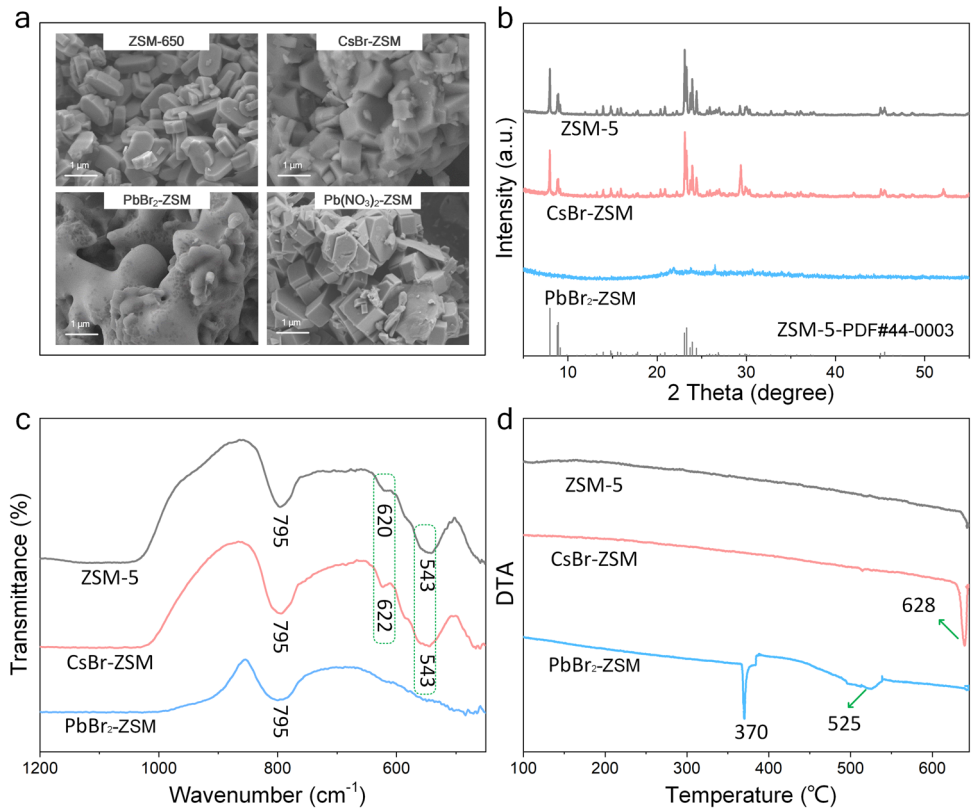

Fig. 3 Morphological and structural evolution of the ZSM-5 matrix annealed with other substances. SEM images of ZSM-650, CsBr-ZSM, $PbBr_2$-ZSM and $Pb(NO_3)_2$-ZSM. **b** XRD patterns, **c** FTIR spectra, and **d** DTA curves of ZSM-5 (gray line), CsBr-ZSM (pink line), and $PbBr_2$-ZSM (blue line).

endothermic peaks for the melting points of $PbBr_2$ (~373 °C) and $CsPbBr_3$ (~563 °C) were identified. The exothermic (~479 °C) and endothermic (~502 °C) peaks might be associated with the reactions that cause the morphological changes in ZSM-5, which is consistent with the result observed from the DTA curve for $PbBr_2$-ZSM.

To further explore the etching reaction, changes in the chemical states of ZSM-5 were monitored by XPS. As shown in Fig. 4a–c, the peaks for Si 2p, O 1s, and Al 2p binding energies with $PbBr_2$-ZSM showed obvious right shifts compared to those for pristine ZSM-5. The Si 2p XPS peak of pristine ZSM-5 was located at 103.6 eV, and that of CsBr-ZSM appeared at 103.5 eV. The Si 2p peak of $PbBr_2$-ZSM showed a 0.8 eV shift from 103.6 to 102.8 eV as a result of silicate formation[32]. The O 1s XPS peaks of pristine ZSM-5 and CsBr-ZSM appeared at 532.7 and 532.5 eV, respectively, whereas that of $PbBr_2$-ZSM was shifted to 531.9 eV. The negative binding energy shifts can be ascribed to changes in the chemical environments of Si–OH species. These results are consistent with previous observations that Pb^{2+} can easily replace protons in Si–O–H aluminosilicates due to the high electronegativity (2.33) of Pb^{2+} and its strong oxygen binding capacity[33]. The slight shifts of the Si 2p and O 1s peaks to lower energies and the shift of the Al 2p peak from CsBr-ZSM to higher energy might be ascribed to weak interactions of the CsBr with ZSM-5. In addition, as shown in Fig. 4d–f, there were obvious Br 3d and Pb 4f signals from $PbBr_2$-ZSM, and only a faint Cs 3d XPS peak was observed for CsBr-ZSM, indicating high efficiencies for entrapment of Pb and Br under specific conditions. Overall, the XPS results suggested that the Si–OH bonds in ZSM-5 reacted with $PbBr_2$ to form "Si–O–PbBr" bonds and the Si–O–Pb–O-Si network at high temperatures, and the additional HBr might contribute to the structural etching and collapse of ZSM-5.

Brunauer–Emmett–Teller (BET) gas absorptiometry was used to investigate the porous structures. As listed in Table S1 in the Supplementary Information, pristine ZSM-5, with a large surface area of 324.4509 $m^2\ g^{-1}$ and a narrow mean pore size of 2.0674 nm, constituted a desirable substrate for loading of functional nanomaterials. After the reaction with $PbBr_2$, the surface area decreased slightly to 266.2026 $m^2\ g^{-1}$, and the pore size and volume increased slightly from 2.0674 to 2.1025 nm and 0.13997 to 0.144903 $cm^3\ g^{-1}$, respectively, due to etching. However, the Green-Z composite had a smaller

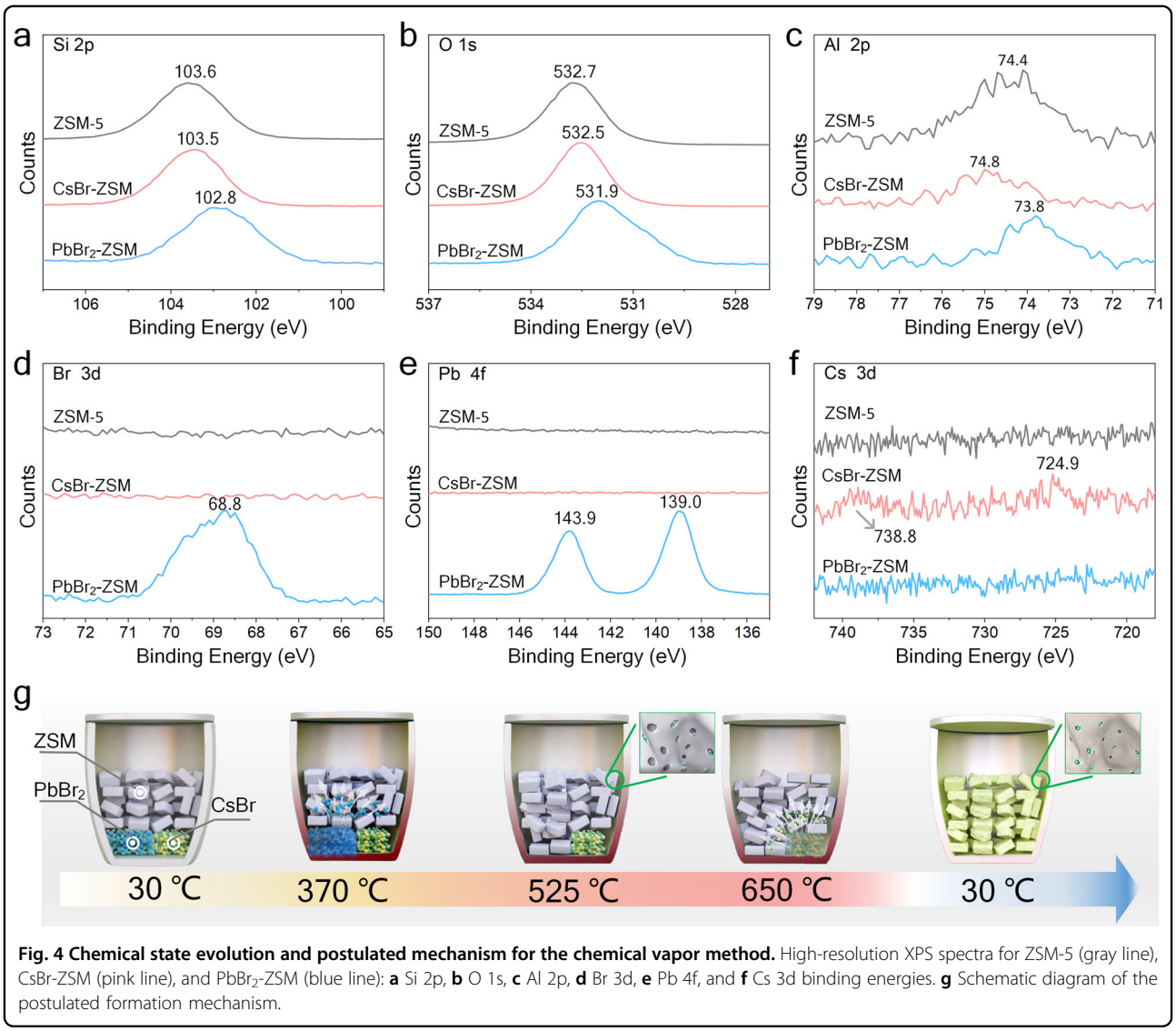

Fig. 4 Chemical state evolution and postulated mechanism for the chemical vapor method. High-resolution XPS spectra for ZSM-5 (gray line), CsBr-ZSM (pink line), and $PbBr_2$-ZSM (blue line): **a** Si 2p, **b** O 1s, **c** Al 2p, **d** Br 3d, **e** Pb 4f, and **f** Cs 3d binding energies. **g** Schematic diagram of the postulated formation mechanism.

surface area (183.3242 m^2 g^{-1}), which decreased with increasing loading, indicating that the $CsPbBr_3$ QDs filled the pores and occupied the spaces. Other than the excessive loading for sample #7 (Fig. S2 in the Supplementary Information), some pores remained in the Green-Z composite to provide channels for halogen exchange. The pore sizes were smaller than the average size for $CsPbBr_3$ QDs distributed in ZSM-5 (~6.4 nm), implying the formation of perovskite in the interrupted structure of the substrate[9,15].

Hence, the mechanism for in situ syntheses of $CsPbX_3$ composites is postulated in Figs. 4g and S13 in the Supplementary Information, and the main reactions are described in Scheme 1 in the Supplementary Information. First, owing to the relatively low melting point, $PbBr_2$ melts in the heating process and moves upward to the pores of ZSM-5 driven by air convection. The H sites in ZSM-5 react with $PbBr_2$ to form HBr, and the remaining $PbBr^+$ or Pb^{2+} binds with Si–O, resulting in incorporation of Pb into the framework. Second, HBr attacks the Si–O bonds and etches channels in the ZSM-5. Subsequently, as the temperature is raised, CsBr reacts with the Si–O–PbBr and $PbBr_2$ trapped by the matrix and intensifies etching at the higher temperatures, which further accelerates the structural collapse of ZSM-5 and seals the $CsPbBr_3$ formed in the channels. During cooling, $CsPbBr_3$ condenses and crystallizes to form QDs in the confined spaces. The remaining channels are responsible for further halogen exchange. A dynamic video clip is included in the Supporting Information to illustrate the process used for syntheses of the $CsPbX_3$-ZSM-5 composites.

Photoluminescence properties and stabilities

The photophysical properties of the $CsPbX_3$-ZSM-5 composites were investigated, and all optical parameters are summarized in Table S2 in the Supplementary Information. First, the absorption and PL emission spectra (Figs. 5a, b and S14 in the Supplementary Information) can be tuned almost across the visible light region simply by changing the halide ratios. Typical Stokes shifts (ΔE_s)

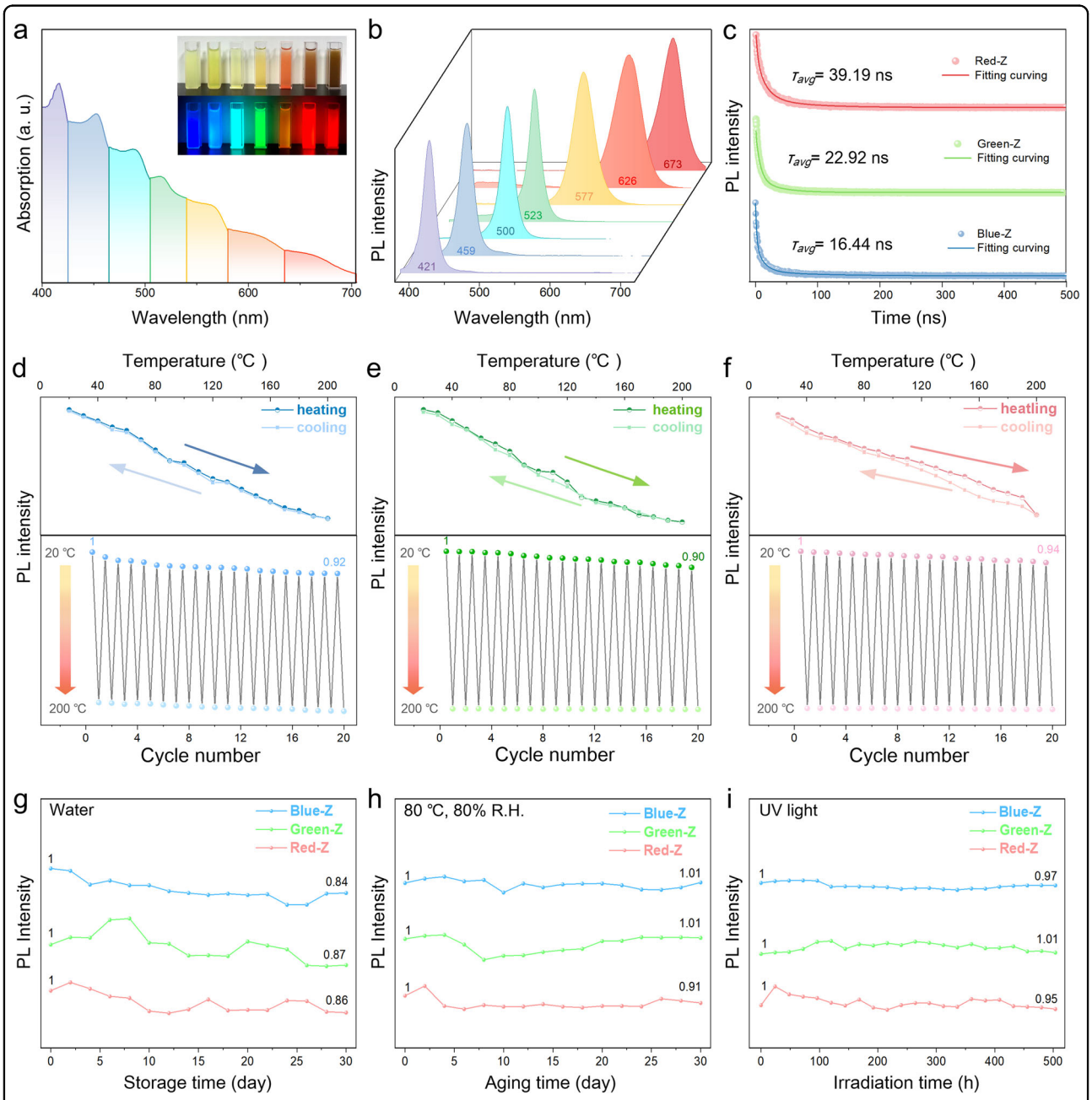

Fig. 5 Photoluminescence properties and stabilities of the synthesized composites. a Absorption spectra of $CsPbX_3$-ZSM-5 from 400 to 700 nm (the inset shows photographs of $CsPbX_3$-ZSM-5 dispersed in glycol under ambient light and 365 nm UV light). **b** PL spectra of $CsPbX_3$-ZSM-5 from 400 to 700 nm. **c** Time-resolved PL decay and fitting curves of the Blue-Z, Green-Z, and Red-Z composites. PL intensity plots: **d** Blue-Z, **e** Green-Z, and **f** Red-Z composites at 20 and 200 °C as a function of cycling number. **g** Water stability evaluation: time-dependent PL intensity of the Blue-Z, Green-Z, and Red-Z composites soaked in water. **h** Aging and stability test: time-dependent PL intensities of the Blue-Z, Green-Z, and Red-Z composites at 80 °C and 80% relative humidity. **i** Photostability test: time-dependent PL intensities of Blue-Z, Green-Z, and Red-Z upon continuous illumination (365 nm).

of approximately 40 meV attributed to perovskite QDs have been observed[34]. Moreover, the narrow emission bands of these composites (with FWHMs from 90 to 143 meV) were comparable to those of solution-synthesized QDs[35]. It should be noted that Green-Z (QD average lengths ~6.4 nm) showed an emission peak at approximately 523 nm, which was a higher wavelength than that previously reported for monodispersed $CsPbBr_3$ nanocubes with edge lengths of 6.3 nm (the emission peak was at approximately 504 nm)[36]. The large difference was probably due to the special packaging and collective effects of the QDs and the molecular sieve matrix, which differed from those of monodispersed QDs formed in solvents. Similar size distributions and PL mismatches have been reported for QDs embedded in glass[37] (sizes averaging 3.8 nm, PL at 516 nm) and $CsPbBr_3$ NCs@mesoporous silica nanospheres[4] (sizes averaging 7.8 nm, PL at 524 nm). With regard to PL efficiency, the PLQY of the Green-Z composite in glycol solution was 92.52% ($\lambda_{ex} = 365$ nm) at room temperature, and those of the Blue-Z and Red-Z composites were approximately 46.24% and 16.91%, respectively (Fig. S15 in the Supplementary Information). Compared to those seen in the glycol dispersions, the PLQYs of Green-Z, Blue-Z, and Red-Z powders showed lower values of 24.11, 5.09, and 4.81%, respectively, which may be due to self-absorption. The time-resolved PL decay spectra of Blue-Z, Green-Z, and Red-Z are shown in Fig. 5c, and the PL decay curves were fitted with tri-exponential decay functions, as shown in Table S3 in the Supplementary Information. The average PL lifetimes of Blue-Z, Green-Z, and Red-Z were 16.44, 22.92, and 39.19 ns, respectively, longer than that of pure perovskite QDs. This could be explained by passivation arising from confined growth in the ZSM-5 structure as well as reduced nonradiative transitions[38]. These results validate the excellent PL properties of the $CsPbX_3$-ZSM-5 composites.

Stability is another vital requirement for commercial applications. The thermal and moisture resistance of the $CsPbX_3$-ZSM-5 composites were first evaluated. An obvious PL decrease and approximately unchanged PL peak positions were observed during heating due to the self-trapping excitons of $CsPbX_3$ (Fig. S16 in the Supplementary Information)[38]. All of the tested composites (Blue-Z, Green-Z, and Red-Z) showed only approximately 50% PL loss during heating from 20 to 100 °C, and 10% of the PL intensity remained even at 200 °C, indicating that the excitons in the $CsPbX_3$-ZSM-5 composites were more thermally stable than those of pure $CsPbX_3$ QDs[39]. As shown in Fig. 5d–f, the PL decrease caused by thermal quenching was recoverable, and the PL intensity was nearly equal to the initial value after cooling to room temperature. In addition, reversible PL was observed when heating the samples from 20 to 200 °C for 20 cycles. The outstanding thermal stability can be ascribed to three main factors. First, ZSM-5 has low thermal conductivity and protects the internal $CsPbX_3$ QDs from high temperatures. Second, confinement within the porous structure of ZSM-5 hinders the aggregation of $CsPbX_3$ QDs at a high temperature. Finally, no ligands were used in the syntheses of the composites, thus avoiding fluorescence damage caused by oxidation and delamination of organic ligands[14].

In the solvent resistance tests, the Blue-Z, Green-Z, and Red-Z composites were immersed in different solvents to monitor PL evolution. Figure 5g shows that after immersion in water for 30 days, Blue-Z, Green-Z, and Red-Z maintained 84, 87, and 86% of their initial PL intensities, respectively. Stability in other solvents was also assessed, as shown in Figs. S17, S18, and S19 in the Supplementary Information. The samples were immersed in ethanol, isopropanol, glycol, dimethylformamide, dimethyl sulfoxide, and acetylacetone, and all of them maintained strong emission intensities after 180 days. The effects of aging are presented in Fig. 5h. The PL intensity of the $CsPbX_3$-ZSM-5 composite was still higher than 90% of the initial value after 30 days of aging at 80 °C under 80% relative humidity (abbreviated as "80 °C, 80% R.H."). To further evaluate the stability under other harsh conditions, the samples were exposed to continuous UV radiation at 365 nm, and the PL intensities exhibited nearly no changes after 500 h (Fig. 5i). The excellent resistance of the $CsPbX_3$-ZSM-5 composites to water, polar solvents, aging, and UV radiation was attributed to protection from ZSM-5, which precluded direct exposure of the $CsPbX_3$ QDs to these external factors and inhibited interparticle fusion of the perovskite nanoparticles. These results provided strong evidence showing that the proposed strategy overcame the inherent instability of $CsPbX_3$ QDs.

Applications for WLEDs and anti-counterfeiting

Because of the advantages of the synthetic strategy, scalable preparation (Fig. 6a) can be easily realized and makes commercialization a possibility. In practice, the use of composites commonly involves organic polymers such as polydimethylsiloxane (PDMS) and polyurethane (PU); therefore, the practicability of these perovskite composites was investigated. Good compatibility with PDMS is indicated in Fig. 6b, and the uniform fluorescent disks emitted bright fluorescence under UV light excitation. In addition, a large-area film measuring 35 cm × 25 cm and made of the Green-Z composite and PU was prepared by screen printing (Fig. S20 in the Supplementary Information).

LEDs are widely recognized as mainstream devices in next-generation backlit displays[20]. Due to their compatibility with polymers, light conversion LED chips can be fabricated by packaging $CsPbX_3$-ZSM-5 composites into

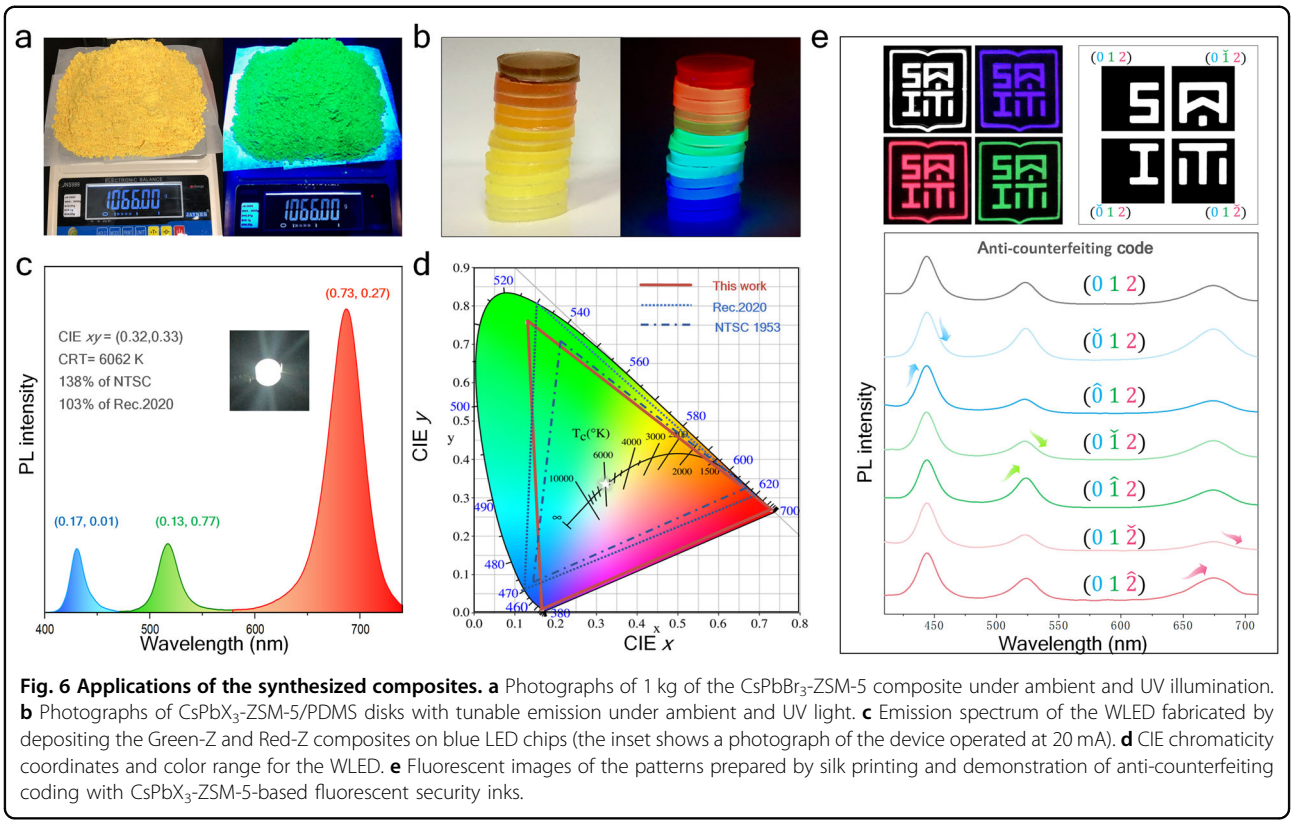

Fig. 6 Applications of the synthesized composites. a Photographs of 1 kg of the $CsPbBr_3$-ZSM-5 composite under ambient and UV illumination. **b** Photographs of $CsPbX_3$-ZSM-5/PDMS disks with tunable emission under ambient and UV light. **c** Emission spectrum of the WLED fabricated by depositing the Green-Z and Red-Z composites on blue LED chips (the inset shows a photograph of the device operated at 20 mA). **d** CIE chromaticity coordinates and color range for the WLED. **e** Fluorescent images of the patterns prepared by silk printing and demonstration of anti-counterfeiting coding with $CsPbX_3$-ZSM-5-based fluorescent security inks.

commercial LED chips. The tolerance of Green-Z and Red-Z packed in the single-wavelength LED chips was evaluated by monitoring the output spectra produced by different driving currents under working conditions. As shown in Fig. S21 in the Supplementary Information, the light intensity had a linear relationship with the current applied. Accordingly, WLEDs were fabricated by combining the Green-Z and Red-Z composites with blue LED chips (430 nm). The emission spectrum of the WLED is presented in Fig. 6c, and the triangle for the CIE color coordinates in the CIE 1931 chromaticity diagram is displayed in Fig. 6d. Three obvious emission peaks were observed at 430, 517, and 687 nm, and the CIE chromaticity coordinates were (0.17, 0.01), (0.13, 0.77), and (0.73, 0.27), respectively. The luminous efficiency of the WLED was 6.8 lm/W at a current of 20 mA. The chromaticity coordinate of the WLED was (0.32, 0.33), and the color temperature (CCT) was 6062 K, close to that of standard white light. The area of the triangle was calculated to be 138% of the National Television System Committee (NTSC) standard and 103% of the ITU-R Recommendation BT.2020 (Rec.2020.), demonstrating an ultrabroad color range.

The $CsPbX_3$-ZSM-5 composites with narrow emission bands and tunable colors also have ample potential for use in security printing technology. Except for the intrinsic UV-excited on/off phenomenon, secondary anti-counterfeiting coding is also quite useful. As mentioned above, the WLEDs exhibited three discrete primary color peaks, thereby providing the possibility of anti-counterfeiting responses coded with the three colors. As shown in Fig. 6e, patterns were printed by blending Blue-Z, Green-Z, and Red-Z with epoxy resin. Similar white emissions with different emission spectra were achieved by mixing the three composites in different ratios, which made it difficult for the naked eye to discern the differences. Therefore, the concept of white light-coded anti-counterfeiting is proposed. The rules for coding were enacted and shown in Fig. 6e. First, blue, green, and red emissions were denoted as "0", "1", and "2", respectively. Second, one of the white light spectra was selected as a reference and encoded as (0 1 2). Finally, the relative increase in a specific peak intensity compared to the reference was denoted as "∧" on the top of the corresponding number; otherwise, it was denoted as "∨". For example, white light with a stronger blue emission peak would be noted as (0̂ 1 2). To assess the practicality, a batch of fluorescent inks exhibiting white emission was prepared, and based on the aforementioned coding rules, symbols were printed with the four different inks, as shown in Fig. 6e. Although all parts of the symbols showed white emission, they had different spectra. These

results revealed the excellent potential of the composites for use in anti-counterfeiting coding.

Conclusions

A novel chemical vapor method was designed and demonstrated for large-scale syntheses of $CsPbX_3$-ZSM-5 composites without the need for organic solvents, organic ligands or an inert environment. Confined growth of $CsPbX_3$ inside the nanopores of ZSM-5 was observed because of reactions between $PbBr_2$ vapor and the Si–O network of ZSM-5, and the resulting encapsulation structure provided the channels needed for halogen exchange. This method offered scalable production of extremely stable composites that exhibited tunable emissions with high PLQYs, narrow emission FWHMs, heat resistance up to 200 °C and radiation resistance, as demonstrated by continuous UV radiation, for 500 h. After immersion in water for 30 days or polar solvents for 180 days, the PL intensity exhibited almost no change. Furthermore, the composites survived aging (80 °C, 80% R.H.) and retained 90% of the initial PL intensity after 30 days. The narrow emissions, high PLQYs and outstanding stability make the $CsPbX_3$-ZSM-5 composites promising for lighting and display applications, especially WLEDs with large color ranges and multicolor-coded anti-counterfeiting inks. This facile, organic-free and ambient atmosphere process indicates the probability for commercial production of these perovskite composites with robust stability.

Acknowledgements

The work was jointly supported by the National Natural Science Foundation of China No. 21975280, Guangdong Provincial Natural Science Foundation No. 2020A1515110831, Shenzhen Science and Technology Research Funding No. JCYJ20180507182047316, Shenzhen Science and Technology Research Funding No. RCJC20200714114435061, National Natural Science Foundation of China No. 62004091, Natural Science Foundation of Guangdong Province No. 2022A1515011959, and City University of Hong Kong Strategic Research Grant No. 7005505.

Author details

[1]Shenzhen Engineering Centre for the Fabrication of Two-Dimensional Atomic Crystals, Shenzhen Institute of Advanced Technology, Chinese Academy of Sciences, Shenzhen 518055, People's Republic of China. [2]University of Chinese Academy of Sciences, Beijing 100049, People's Republic of China. [3]Department of Physics, Department of Materials Science and Engineering, and Department of Biomedical Engineering, City University of Hong Kong, Tat Chee Avenue, Kowloon, Hong Kong, People's Republic of China

Author contributions

H.H. and X.-F.Y. conceived the original research idea. Experiments, including $CsPbX_3$-ZSM composite syntheses, $CsPbX_3$-ZSM-5/PDMS disks, LED packing, anti-counterfeiting ink preparation and stability tests, were performed by T.Y.S. and X.C., Y.H.D., H.H., J.H.W., R.H., and Y.L.L. X.C.H. carried out the characterizations, and J.L. assisted with data analysis. T.Y.S., X.C., H.H., P.K.C., and X.-F.Y. wrote this manuscript. All authors discussed the results, interpreted the findings, and commented on the manuscript.

Competing interests

The authors declare no competing interests.

Supplementary information The online version contains supplementary material available at https://doi.org/10.1038/s41427-022-00433-0.

Received: 12 April 2022 Revised: 8 September 2022 Accepted: 14 September 2022.
Published online: 4 November 2022

References

1. Smock, S. R., Chen, Y., Rossini, A. J. & Brutchey, R. L. The surface chemistry and structure of colloidal lead halide perovskite nanocrystals. *Acc. Chem. Res.* **54**, 707–718 (2021).
2. Yu, J. et al. Perovskite $CsPbBr_3$ crystals: Growth and applications. *J. Mater. Chem. C* **8**, 6326–6341 (2020).
3. Kovalenko, M. V., Protesescu, L. & Bodnarchuk, M. I. Properties and potential optoelectronic applications of lead halide perovskite nanocrystals. *Science* **358**, 745–750 (2017).
4. Yu, X. et al. Hydrochromic $CsPbBr_3$ nanocrystals for anti-counterfeiting. *Angew. Chem., Int. Ed.* **59**, 14527–14532 (2020).
5. Smith, M. D., Connor, B. A. & Karunadasa, H. I. Tuning the luminescence of layered halide perovskites. *Chem. Rev.* **119**, 3104–3139 (2019).
6. Pan, A. et al. Insight into the ligand-mediated synthesis of colloidal $CsPbBr_3$ perovskite nanocrystals: the role of organic acid, base, and cesium precursors. *ACS Nano* **10**, 7943–7954 (2016).
7. Shamsi, J., Urban, A. S., Imran, M., De Trizio, L. & Manna, L. Metal halide perovskite nanocrystals: synthesis, post-synthesis modifications, and their optical properties. *Chem. Rev.* **119**, 3296–3348 (2019).
8. Zhang, S. et al. Barrier designs in perovskite solar cells for long-term stability. *Adv. Energy Mater.* **10**, 2001610 (2020).
9. Tong, Y. et al. One-pot synthesis of $CsPbX_3$ (X = Cl, Br, I)@zeolite: A potential material for wide-color-gamut backlit displays and upconversion emission. *Adv. Opt. Mater.* **9**, 2100012 (2021).
10. Wei, Y., Cheng, Z. & Lin, J. An overview on enhancing the stability of lead halide perovskite quantum dots and their applications in phosphor-converted LEDs. *Chem. Soc. Rev.* **48**, 310–350 (2019).
11. Yin, J. et al. Luminescence and stability enhancement of inorganic perovskite nanocrystals via selective surface ligand binding. *ACS Nano* **15**, 17998–18005 (2021).
12. Lin, Y. et al. All-inorganic encapsulation for remarkably stable cesium lead halide perovskite nanocrystals: toward full-color display applications. *J. Mater. Chem. C* **9**, 12303–12313 (2021).
13. Lin, Y. et al. Remarkable black-phase robustness of $CsPbI_3$ nanocrystals sealed in solid SiO_2/AlO_x sub-micron particles. *Small* **17**, 2103510 (2021).
14. Zhang, Q. et al. Ceramic-like stable $CsPbBr_3$ nanocrystals encapsulated in silica derived from molecular sieve templates. *Nat. Commun.* **11**, 31 (2020).
15. Wang, P. et al. Ultrastable perovskite–zeolite composite enabled by encapsulation and in situ passivation. *Angew. Chem., Int. Ed.* **59**, 23100–23106 (2020).
16. Sun, J.-Y. et al. Facile two-step synthesis of all-inorganic perovskite $CsPbX_3$ (X = Cl, Br, I) zeolite-Y composite phosphors for potential backlight display application. *Adv. Funct. Mater.* **27**, 1704371 (2017).
17. Ravi, V. K., Saikia, S., Yadav, S., Nawale, V. V. & Nag, A. $CsPbBr_3$/ZnS core/shell type nanocrystals for enhancing luminescence lifetime and water stability. *ACS Energy Lett.* **5**, 1794–1796 (2020).
18. Imran, M. et al. Halide perovskite–lead chalcohalide nanocrystal heterostructures. *J. Am. Chem. Soc.* **143**, 1435–1446 (2021).
19. Wang, Z. et al. One-step polymeric melt encapsulation method to prepare $CsPbBr_3$ perovskite quantum dots/polymethyl methacrylate composite with high performance. *Adv. Funct. Mater.* **31**, 2010009 (2021).
20. Yang, W. et al. $CsPbBr_3$-quantum-dots/polystyrene@silica hybrid microsphere structures with significantly improved stability for white LEDs. *Adv. Opt. Mater.* **7**, 1900546 (2019).
21. Qiao, G.-Y. et al. Perovskite quantum dots encapsulated in a mesoporous metal–organic framework as synergistic photocathode materials. *J. Am. Chem. Soc.* **143**, 14253–14260 (2021).

22. Wan, S., Ou, M., Zhong, Q. & Wang, X. Perovskite-type $CsPbBr_3$ quantum dots/Uio-66(NH_2) nanojunction as efficient visible-light-driven photocatalyst for CO_2 reduction. *Chem. Eng. J.* **358**, 1287–1295 (2019).
23. Hou, J. et al. Liquid-phase sintering of lead halide perovskites and metal-organic framework glasses. *Science* **374**, 621–625 (2021).
24. Jang, J. et al. Extremely stable luminescent crosslinked perovskite nanoparticles under harsh environments over 1.5 years. *Adv. Mater.* **33**, 2005255 (2021).
25. Li, X. et al. Chemical vapor deposition for N/S-doped single Fe site catalysts for the oxygen reduction in direct methanol fuel cells. *ACS Catal.* **11**, 7450–7459 (2021).
26. Wang, H. & Yu, G. Direct CVD graphene growth on semiconductors and dielectrics for transfer-free device fabrication. *Adv. Mater.* **28**, 4956–4975 (2016).
27. Almutairi, S. M. T., Mezari, B., Magusin, P. C. M. M., Pidko, E. A. & Hensen, E. J. M. Structure and reactivity of Zn-modified ZSM-5 zeolites: The importance of clustered cationic Zn complexes. *ACS Catal.* **2**, 71–83 (2012).
28. Ou, X. et al. Hierarchical Fe-ZSM-5/SiC foam catalyst as the foam bed catalytic reactor (FBCR) for catalytic wet peroxide oxidation (CWPO). *Chem. Eng. J.* **362**, 53–62 (2019).
29. Kübel, C. et al. Recent advances in electron tomography: TEM and HAADF-STEM tomography for materials science and semiconductor applications. *Microsc. Microanal.* **11**, 378–400 (2005).
30. Coudurier, G., Naccache, C. & Vedrine, J. C. Uses of I.R. spectroscopy in identifying ZSM zeolite structure. *J. Chem. Soc., Chem. Commun.* **24**, 1413–1415 (1982).
31. Isernia, L. F. FTIR study of the relation, between extra-framework aluminum species and the adsorbed molecular water, and its effect on the acidity in ZSM-5 steamed zeolite. *Mater. Res.* **16**, 792–802 (2013).
32. Wang, H. et al. Encapsulating silica/antimony into porous electrospun carbon nanofibers with robust structure stability for high-efficiency lithium storage. *ACS Nano* **12**, 3406–3416 (2018).
33. Selim, A. Q. et al. Statistical physics-based analysis of the adsorption of Cu^{2+} and Zn^{2+} onto synthetic cancrinite in single-compound and binary systems. *J. Environ. Chem. Eng.* **7**, 103217 (2019).
34. Brennan, M. C. et al. Universal size-dependent Stokes shifts in lead halide perovskite nanocrystals. *J. Phys. Chem. Lett.* **11**, 4937–4944 (2020).
35. Nedelcu, G. et al. Fast anion-exchange in highly luminescent nanocrystals of cesium lead halide perovskites ($CsPbX_3$, X = Cl, Br, I). *Nano Lett.* **15**, 5635–5640 (2015).
36. Imran, M. et al. Shape-pure, nearly monodispersed $CsPbBr_3$ nanocubes prepared using secondary aliphatic amines. *Nano Lett.* **18**, 7822–7831 (2018).
37. Huang, X. et al. Reversible 3D laser printing of perovskite quantum dots inside a transparent medium. *Nat. Photonics* **14**, 82–88 (2020).
38. Li, X. et al. $CsPbBr_3$ quantum dots for lighting and displays: Room-temperature synthesis, photoluminescence superiorities, underlying origins, and white light-emitting diodes. *Adv. Funct. Mater.* **26**, 2435–2445 (2016).
39. Wei, Y. et al. Epitaxial growth of $CsPbX_3$ (X = Cl, Br, I) perovskite quantum dots via surface chemical conversion of Cs_2GeF_6 double perovskites: a novel strategy for the formation of leadless hybrid perovskite phosphors with enhanced stability. *Adv. Mater.* **31**, 1807592 (2019).